Received: 27 December 2023 | Revised: 1 July 2024 | Accepted: 8 July 2024

DOI: 10.1002/elan.202300422

RESEARCH ARTICLE

ELECTROANALYSIS

# Plant-assisted synthesis of $Fe_3O_4$ nanoparticles for catalytic degradation of methyl orange dye and electrochemical sensing of nitrite

**Siti Husnaa Mohd Taib**[1] | **Pooria Moozarm Nia**[2] | **Roshafima Rasit Ali**[1] | **Zahra Izadiyan**[1] | **Zatil Izzah Tarmizi**[1] | **Kamyar Shameli**[3]

[1]Malaysia-Japan International Institute of Technology (MJIIT), Universiti Teknologi Malaysia, Kuala Lumpur, Malaysia

[2]Department of Biological and Chemical Engineering, Aarhus University, Aarhus, Denmark

[3]School of Medicine, Technical University of Munich, Munich Germany

**Correspondence**
Kamyar Shameli, School of Medicine, Technical University of Munich, Munich Germany.
Email: kamyarshameli@gmail.com and kamyar.shameli@tum.de

**Abstract**

The present study details a more environmentally friendly method for synthesizing iron oxide nanoparticles ($Fe_3O_4$-NPs) utilizing *Hibiscus sabdariffa* (*H. sabdariffa*) leaf extract. The produced *H. sabdariffa*/$Fe_3O_4$-NPs underwent characterization through VSM, XRD, FESEM-EDX, TEM and FTIR analyses. The FESEM and TEM images revealed that the *H. sabdariffa*/$Fe_3O_4$-NPs had a narrow distribution and an average particle size of $5 \pm 2$ nm. Catalytic degradation studies of the synthesized $Fe_3O_4$-NPs exhibited efficient reduction of methyl orange (MO) dye. The degradation of MO catalysed by *H. sabdariffa*/$Fe_3O_4$-NPs follow the pseudo-first order kinetics, with a rate constant of 0.0328 $s^{-1}$ ($R2 = 0.9866$). Moreover, in electrochemical sensing studies, the anodic peak current of nitrite ($NO_2^-$) for *H. sabdariffa*/$Fe_3O_4$-NPs/GCE showed a linear relationship with its concentration within the range of 0.5–7.5 mM, achieving a detection limit of 0.29 μM. These findings demonstrate that the modified electrode with $Fe_3O_4$-NPs synthesized using *H. sabdariffa* leaf extract serve as a novel electrochemical sensor for determining $NO_2^-$ with high sensitivity and reproducibility.

**KEYWORDS**
catalytic degradation, electrooxidation, glassy carbon electrode, iron oxide nanoparticles, nitrite sensor

## 1 | INTRODUCTION

Recently, magnetic nanoparticles (NPs), especially iron oxide ($Fe_3O_4$) NPs have received considerable attention because of their unique properties, such as the high surface-to-volume ratio, low toxicity, easy synthesis, electrocatalytic capability and superparamagnetic [1,2]. Research on the utilization of $Fe_3O_4$-NPs for catalysis, memory storage devices, sensors, drug delivery, magnetic resonance imaging and treatment of cancer cells has been explored and is still ongoing [3]. The ability to synthesize $Fe_3O_4$-NPs is important for exploring their unique properties in sensor and catalytic degradation applications. Numerous methods of producing $Fe_3O_4$-NPs have been developed to achieve the desired properties. This is including the chemical precipitation method that involves the co-precipitation of ferric and ferrous ions by sodium hydroxide or ammonia solution,

the sol-gel method, sono-chemical synthesis, solvothermal synthesis, and thermal decomposition [4–9]. However, success in precise particle size control of $Fe_3O_4$-NPs has only been achieved through thermal decomposition using large quantities of toxic and expensive precursors and surfactants in an organic solvent. Therefore, a green method for the synthesis of NPs could be plant extract usage, which possesses various advantages such as cost-efficiency, safety, simplicity, and non-toxicity [10,11]. The use of plant extract in the green synthesis of $Fe_3O_4$-NPs has recently been expanded in a variety of fields. For example, *Citrus medica* L. var. *sarcodactylis* Swingle has been used to synthesize of $Fe_3O_4$-NPs for river water treatment [12]. In addition, separation of toxic metals and dyes from the environment using $Fe_3O_4$-NPs that synthesized by plantain has been also reported [13]. In the present work, *Hibiscus sabdariffa* (*H. sabdariffa*) leaves extract was used as reducing and stabilizing agents in the synthesis of $Fe_3O_4$-NPs. *H. sabdariffa* is an herb plant that has been found to have antibacterial, diuretic, antioxidant, antidiabetic, anti-cholesterol, chemo-protective, anti-hypertensive, blood pressure suppressive, antitumor, and anticancer properties [14]. Furthermore, Karim and colleagues evaluated the potential of *H. sabdariffa* calyx as a sensing material by immobilizing delphinidin-3-sambubioside in glass fibre filter paper [15]. The delphinidin-3-sambubioside is a natural reddish colour compound that can easily be found in *H. sabdariffa* calyx. According to the findings, natural colour extract compound present in *H. sabdariffa* calyx can be used as a sensing material in the development of an optical pH sensor. On the synthesis of $Fe_3O_4$-NPs utilising the leaf extract of *H. sabdariffa*, very little is known. Hence, this study aims to explore the formation of $Fe_3O_4$-NPs by *H. sabdariffa* leaf extract and assess the effectiveness of the synthesized $Fe_3O_4$-NPs act as catalyst in degrading of methyl orange (MO) dye and electrooxidizing detection of nitrite ($NO_2^-$).

Protecting the environment is crucial, given that pollutants like dyes produced daily by textile industries are highly toxic, carcinogenic, mutagenic, and non-biodegradable [16]. One such toxic azo dye is MO, a water-soluble, heterocyclic aromatic chemical compound with the molecular formula $C_{14}H_{14}N_3NaO_3S$. Exposure to MO can cause diarrhoea, nausea and can be fatal [17]. Additionally, industrial dyes pose challenges due to their stability and toxicity, making the development of advanced catalyst crucial for degradation processes [18]. Therefore, we investigated the catalytic properties of *H. sabdariffa*/$Fe_3O_4$-NPs for degrading MO in water using UV-vis spectroscopy.

In addition, $NO_2^-$ is an inorganic compound that possesses both environmental and biological importance that can be easy to find in our diet, through drinking water and vegetables. The consumption of high concentrations of $NO_2^-$, is undoubtedly toxic to humans. $NO_2^-$ can interact with haemoglobin to create methaemoglobin, resulting in methemoglobinemia (blue baby syndrome), which poses a risk to human health, particularly for infants, due to a decrease in the oxygen-carrying capabilities of the blood [19,20]. The presence of $NO_2^-$ in the environment, an increasing need for better industrial process control, developments in clinical diagnostics and various areas have led to the search for low cost, fast response, and high sensitivity methods for detection of $NO_2^-$.

Different methods have been used to determine $NO_2^-$, including spectrophotometry, chromatography, chemiluminescence, capillary electrophoresis, and electrochemical methods [21–27]. Electrochemical techniques have advantages over other methods in terms of low cost, quick response, and high sensitivity [28]. $NO_2^-$ can be examined electrochemically using the electrooxidation or electroreduction processes. When $NO_2^-$ is examined by electrooxidation, the effect of dissolved oxygen is eliminated [29]. Even so, during $NO_2^-$ detection, the regular electrode has a significant electrooxidation overpotential. Furthermore, the electrode may be destructed by the products produced during the electrochemical reaction, reducing electrode accuracy and sensitivity [30]. So, it is the key factor to seek for the new modified electrode. Ever since, researchers have become interested in the alteration of working electrodes by nanomaterials [31–33]. Therefore, in this work, $Fe_3O_4$-NPs have been chosen to coat on the surface of the electrode to solve the problems and improve the electrode performance in $NO_2^-$ determination. This arises from the extensive surface area of $Fe_3O_4$-NPs (ranging from 10–50 $m^2 g^{-1}$), intriguing electronic characteristics, superior mechanical resilience, and remarkable stability, as documented in reference by Urbanova et al. [34]. In this study, the objectives were multi-faceted. Firstly, it aimed to highlight the growing significance of magnetic nanoparticles, particularly $Fe_3O_4$-NPs, due to their unique properties and versatile applications in various fields, including catalysis and environmental remediation. Secondly, it underscored the exploration of green synthesis routes utilizing plant extracts, specifically focusing on *H. sabdariffa*, to synthesize $Fe_3O_4$-NPs with a narrow size distribution, aiming to replace conventional methods involving toxic chemicals. Thirdly, it sought to investigate the catalytic effectiveness of $Fe_3O_4$-NPs in degrading toxic pollutants like MO dye, contributing to environmental protection efforts. Finally, the text aimed to explore the potential of $Fe_3O_4$-NPs modified electrodes for electrochemical detection of nitrite ($NO_2^-$), addressing the need

for low-cost, sensitive, and efficient methods for $NO_2^-$ determination, which was crucial for environmental monitoring and human health protection.

## 2 | MATERIALS AND METHOD

### 2.1 | Materials

The precursors of Iron (III) chloride hexahydrate ($FeCl_3.6H_2O$), 97% and Iron (II) chloride tetrahydrate ($FeCl_2.4H_2O$), ≥99% were obtained from Sigma Aldrich, USA. Potassium chloride (KCl), sodium nitrite ($NaNO_2$) and sodium hydroxide (NaOH), 99% were procured from R&M chemicals. The reagents used in the reaction were all analytical grade and of high purity.

### 2.2 | Method

#### 2.2.1 | Synthesis of *H. sabdariffa*/Fe3O4-NPs

Hibiscus sabdariffa leaf extract was prepared using a previously reported method [32]. The synthesis of *H. sabdariffa*/$Fe_3O_4$-NPs involved adding a 2:1 M solution of $FeCl_3.6H_2O$ and $FeCl_2.4H_2O$ to the leaf extract, followed by dropwise addition of freshly prepared 2.0 M NaOH while stirring continuously until reaching a pH of 12. The resulting solution was stirred further for 15 min, and the *H. sabdariffa*/$Fe_3O_4$-NPs were separated using a permanent magnet, washed with deionized water, and dried in an oven at approximately 70 °C for 24 hours for subsequent analysis.

#### 2.2.2 | Characterization of synthesized *H. sabdariffa*/Fe3O4-NPs

The magnetic characteristics of *H. sabdariffa*/$Fe_3O_4$-NPs were evaluated using a vibrating sample magnetometer (VSM) at room temperature. (VSM, Lakeshore/7404). X-ray diffraction (XRD) analysis was conducted using a PANalytical X'pert Pro MPD diffractometer with Cu Kα (λ = 1.5406) in the 2Θ range from 10°–90° to determine crystallinity. Surface morphology and element distribution were observed using FESEM-EDX (JEOL-JSM-7600F). To further confirm the morphology and size of the *H. sabdariffa*/$Fe_3O_4$-NPs, an aqueous dispersion of the prepared $Fe_3O_4$-NPs was dip-coated onto a carbon-coated copper grid, dried, and then visualized using the JEOL JEM-2100F TEM (200 kV). The functional group present in the synthesized NPs was analysed by FTIR (Thermo Scientific Nicolet FTIR 6700, United States).

#### 2.2.3 | Catalytic degradation of methyl orange

The catalytic activity of the synthesized $Fe_3O_4$-NPs in degrading methyl orange (MO) was assessed in the range of 220–800 nm using a UV-vis spectrophotometer (UV − 1800, Shimadzu, Japan). Experiments on the degradation of MO in aqueous media which involves the mixing of 3 mL of the MO (10 ppm) with 0.5 mL freshly prepared $NaBH_4$ (0.6 M) solution and 0.025 g *H. sabdariffa*/$Fe_3O_4$-NPs in a quartz cuvette were performed under reaction time of 0–50 min. The percent degradation of MO was calculated using following equation:

$$\%\ \text{Degradation} = \left[1 - \frac{A_0}{A_t}\right] \times 100$$

Where $A_0$ is the initial MO absorbance at 0 min and $A_t$ is the absorbance at times taken for degradation of MO.

#### 2.2.4 | Preparation and modification of electrode

First, the surface of the glassy carbon electrode (GCE) was mechanically cleaned by polishing with 0.3–0.05 μm alumina ($Al_2O_3$) polishing suspension on micro-cloth pads. To get rid of stuck-on $Al_2O_3$ particles, deionized water was used to rinse the electrode surface. After that, the electrode was sonicated in a mixture of ethyl alcohol and water (50:50, v/v), it is rinsed again with deionized water, then the electrode was dried. Prior to use, 1 mg of $Fe_3O_4$-NPs powder was dissolved in 1 mL of chitosan. Before depositing the NPs on GCE, all dispersion solutions were sonicated for 30 min in an ultrasonic bath to create a stable suspension. To investigate the effect of drop casting method, different volumes of $Fe_3O_4$-NPs suspensions (5–35 μL) was deposited on the GCE (act as a working electrode) and then the modified GCE was dried in an oven at 55 °C for 6 hours before electrochemical behaviour experiments.

#### 2.2.5 | Electrochemical performance analysis

For the electrochemical characterization of the *H. sabdariffa*/$Fe_3O_4$-NPs, cyclic voltammogram (CVs) and chronoamperometry data were obtained by a

potentiostat (VersaSTAT 3, AMETEK) operated by VersaStudio software, using a conventional three-electrode setup. The working electrodes were a GCE with a diameter of 3 mm modified with the *H. sabdariffa*/$Fe_3O_4$-NPs. The reference electrode and counter electrodes were made of a saturated calomel reference electrode (SCE) and platinum wire, respectively. The CVs were observed at a scan rate of 50 $mVs^{-1}$ in 1 mM $NO_2^-$ + 0.1 M KCl.

## 3 | RESULTS AND DISCUSSION

### 3.1 | Vibrating-sample magnetometer (VSM) analysis

The magnetic behaviour of synthesized $Fe_3O_4$-NPs was investigated using VSM analysis. The magnetization curve of *H. sabdariffa*/$Fe_3O_4$-NPs at room temperature is shown in Figure 1. The hysteresis loop of VSM analysis of *H. sabdariffa*/$Fe_3O_4$-NPs at room temperature shows saturation magnetization ($M_s$) value of 19.00 emu/g, coercivity ($H_c$) value of 17.33 G, and remanent magnetization ($M_r$) value of about 0.08 emu/g. The magnetic properties of materials were strongly dependent on their grain size and structure [35]. In this study, the $M_s$ values were lower than the bulk $Fe_3O_4$ (92 emu/g), which can be attributed to the much smaller size of $Fe_3O_4$-NPs [36]. The negligibly small $M_r$ of the synthesized $Fe_3O_4$- NPs confirmed their superparamagnetic character [37].

### 3.2 | X-ray diffraction (XRD) analysis

The crystallinity and phase purity of the synthesized $Fe_3O_4$-NPs were investigated using XRD analysis. The XRD patterns of *H. sabdariffa* leaves extract and synthesized $Fe_3O_4$-NPs were shown in Figure 2(a,b). The XRD spectrum of *H. sabdariffa* leaves extract (Figure 2a) revealed only a broad diffraction peak at 26.40° due to the amorphous nature of the plant [38]. Diffraction peaks of synthesized $Fe_3O_4$-NPs were observed in at 2Θ values of 30.64° (220), 35.87° (311), 43.98° (400), 57.55° (422), and 62.36° (511). The formation of crystalline $Fe_3O_4$-NPs is indicated by these peaks. All the peaks were matched to the standard $Fe_3O_4$ XRD pattern, JCPDS file no. 00–019-0629. Estimation of the crystallite size of synthesized $Fe_3O_4$-NPs can be calculated from XRD data using Debye-Scherrer equation [39,40]. The average crystallite size of *H. sabdariffa*/$Fe_3O_4$-NPs from (311) reflection was calculated to be 4.36 nm.

### 3.3 | Morphology study

FESEM-EDX analysis was carried out to study the surface morphology and elemental characteristics of *H. sabdariffa* leaves extract and synthesized $Fe_3O_4$-NPs. Figure 3a show the FESEM image of the *H. sabdariffa* leaves extract in magnification of X20,000 which has an irregular and uneven surface. The NPs were also not observed on the surface of *H. sabdariffa* leaf extract. Figure 3b shows the EDX spectrum of *H. sabdariffa* leaves extract with high peaks of carbon (C), oxygen (O) and aluminium (Al) elements were observed. These peaks are related to the organic biomolecules present in *H. sabdariffa* leaf extract, where the peak appeared at 1.5 keV and corresponded with Al that came from the sample preparation on the Al surface. Figure 3(c and e) shows the FESEM images of the *H. sabdariffa*/$Fe_3O_4$-NPs in magnification of X20,000, and X150,000 which reveals that a $Fe_3O_4$-NPs seems to be almost spherical in morphology. The most important part of this section is the EDX analysis (Figure 3d and f), which in the presence of

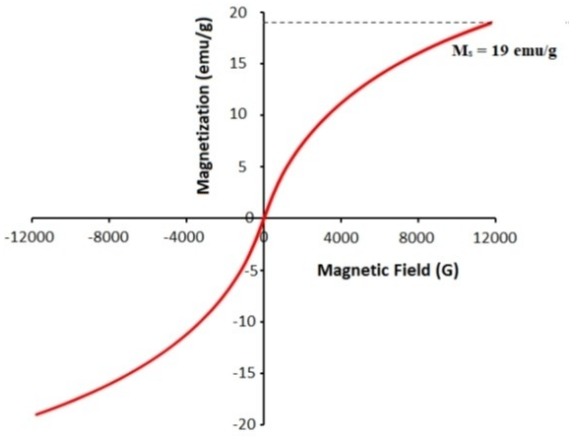


FIGURE 1 VSM plot of *H. sabdariffa*/$Fe_3O_4$-NPs at room temperature.

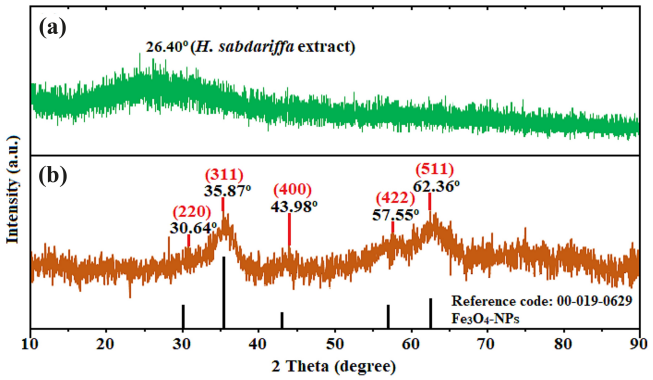


FIGURE 2 XRD patterns of (a) *H. sabdariffa* leaves extract and (b) synthesized $Fe_3O_4$-NPs.

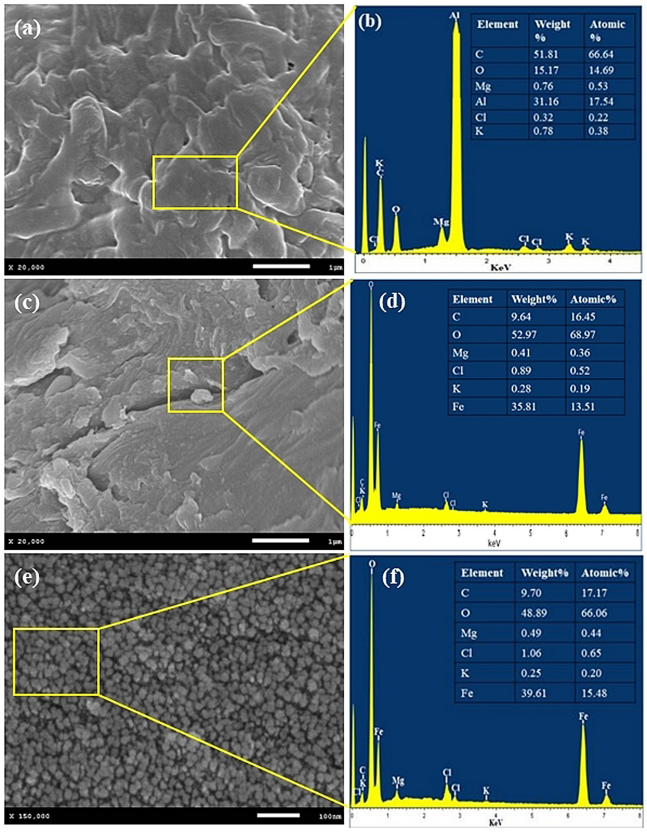


**FIGURE 3** FESEM micrograph of (a) *H. sabdariffa* leaves extract, synthesized $Fe_3O_4$-NPs at (c) 20,000x magnification and x150,000x magnification. EDX spectra of of (b) *H. sabdariffa* leaves extract, synthesized $Fe_3O_4$-NPs at (d) 20,000x and (f) based on analysed area in yellow box.

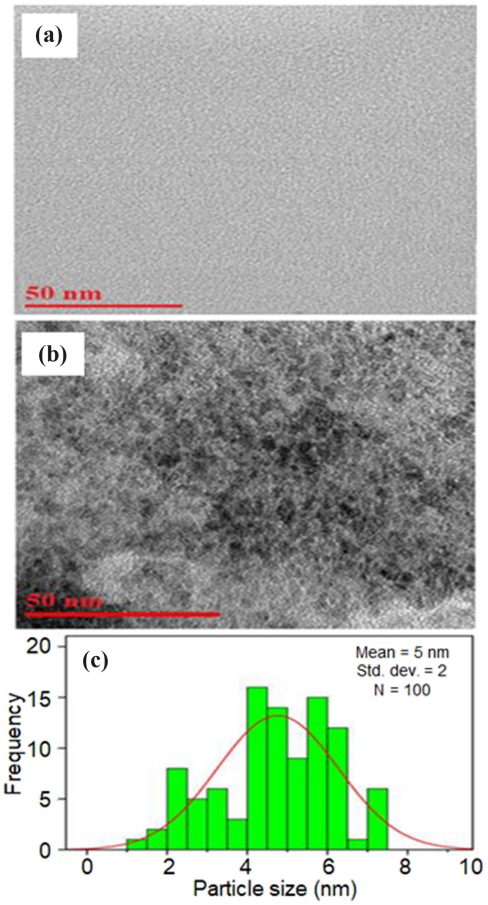


**FIGURE 4** TEM image of (a) 50 nm blank scale for *H. sabdariffa* leave extract as a control and (b) synthesized $Fe_3O_4$-NPs. (c) Particle size distribution of synthesized $Fe_3O_4$-NPs with average size was 5 nm based on Gaussian curve (red line).

significant peaks of Fe and O revealed the formation of $Fe_3O_4$-NPs. The three peaks can be observed around 0.7, 6.4, and 7.1 keV have corresponded to the binding energies of Fe [41].

The spectrums contained three main peaks, which were assigned to Fe, O, and C. Thus, the formation of $Fe_3O_4$-NPs was confirmed. In the EDX spectrum, the O element appears as a strong signal. This suggested that the existence polyphenol compound in *H. sabdariffa* leaf extract is attached to the surface of $Fe_3O_4$-NPs. In addition, the presence of trace amounts of Mg, Cl, d K in the sample might be due to mineral composition from *H. sabdariffa* leaves extract [14].

The size and morphology of the synthesized $Fe_3O_4$-NPs were further analysed by using TEM. The size of NPs is obtained by using ImageJ software to measure the diameter of NPs. Figure 4a show a TEM image of *H. sabdariffa* leaf extract. Due to the high-resolution TEM and characteristics of plant extract, it was unable to measure the particle size. Hence, Figure 4a was used as a control in the experiment.

The TEM image and particles size distribution of $Fe_3O_4$-NPs are shown in Figure 4(b and c), respectively. The TEM image of particles obtained was found to be spherical with an average particle radius of $5 \pm 2$ nm based on the measurement of 100 particles which shows good agreement with the XRD result (4.36 nm). According to the TEM images, the agglomeration has occurred in some of $Fe_3O_4$-NPs. The agglomeration is due to the van der Waals force between particles [42].

## 3.4 | Fourier transform infrared spectroscopy (FTIR) analysis

The FTIR analysis was performed to identify the potential organic compounds in the *H. sabdariffa* leaves extract that is responsible for the efficient reduction and stabilization of NPs. Figure 5a shows the FTIR spectrum for the extract of *H. sabdariffa* leaves. The stretching vibration of the −OH group attached to the aromatic ring structures of flavonoids compounds in the *H. sabdariffa*

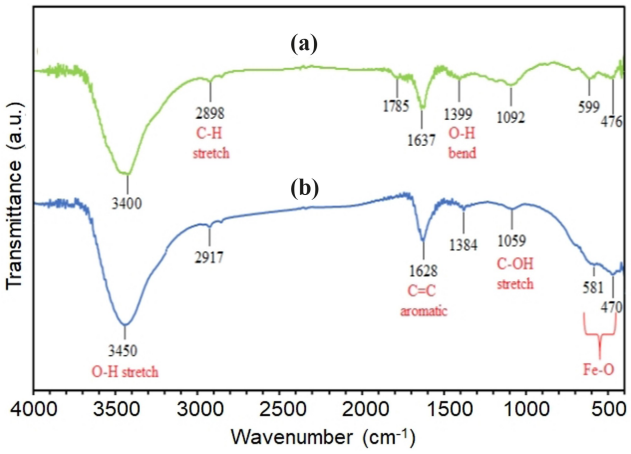


**FIGURE 5** FTIR spectra of (a) *H. sabdariffa* leaves extract and (b) synthesized $Fe_3O_4$-NPs.

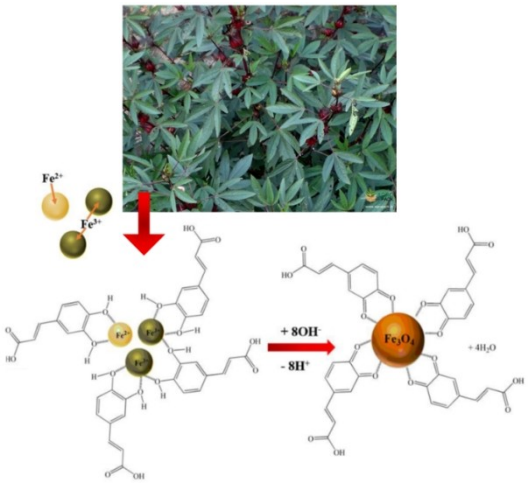


**FIGURE 6** Mechanism of the formation of $Fe_3O_4$-NPs by caffeic acid compound present in *H. sabdariffa* leaves extract.

leaves extract causes a strong intense absorption band at 3400 $cm^{-1}$ [43]. The spectrum of *H. sabdariffa* leaves extract also showed other peaks at 2898, 1785, 1637, 1399, and 1092 $cm^{-1}$ which corresponds to the C—H stretch methylene groups, C=O groups, C=C aromatic stretch, O—H bending, and C—OH stretch, respectively. These peaks are related to the caffeic acid component present in the *H. sabdariffa* leaves extract which shows the same band with natural extract from previous reports [44,45].

Contrary, in Figure 5b, the presence of $Fe_3O_4$-NPs can be seen by two strong absorption bands at around 581 and 470 $cm^{-1}$ which, corresponding to the Fe—O stretching band of bulk $Fe_3O_4$ [46,47]. Both the *H. sabdariffa* leaves extract and synthesized $Fe_3O_4$-NPs illustrate an almost similar FTIR spectrum. However, a slight shift in the peaks and the intensity of the peaks increase in $Fe_3O_4$-NPs spectrum indicates the successful attachment of the *H. sabdariffa* leaves extract to the surface of $Fe_3O_4$-NPs. Besides, for synthesized $Fe_3O_4$-NPs, a small shift of the band to 3450 $cm^{-1}$ was noticed, which indicated that the synthesis process of $Fe_3O_4$-NPs is likely to have involved the -OH functional group.

## 3.5 | Suggested mechanism of *H. sabdariffa*/$Fe_3O_4$-NPs formation

Figure 6 illustrates a schematic representation of the possible mechanism for the synthesizing $Fe_3O_4$-NPs through this environmentally friendly method, leveraging the caffeic acid moiety of chlorogenic acid as a representative of the flavonoid compounds found in *H. sabdariffa* leaves, as reported in previous studies [48]. Initially, $Fe^{3+}$, $Fe^{2+}$ and *H. sabdariffa* leaves extract coexist in an aqueous phase within the reaction system. Within this system, $Fe^{3+}$ and $Fe^{2+}$ can create a 5-membered chelate ring by utilizing the ortho-dihydroxyl groups of the caffeic acid. Then, the addition of NaOH involves $OH^-$ in the reaction, resulting in the formation of ferric hydroxide, $Fe(OH)_3$, and ferrous hydroxide, $Fe(OH)_2$. The formation of $Fe(OH)_3$ and $Fe(OH)_2$ leads to a shell-core structure with caffeic acid acting as the shell. Subsequently, dehydration ($-H_2O$) of $Fe(OH)_3$ and $Fe(OH)_2$ within the core generates $Fe_3O_4$-NPs [47]. The chelated ortho-dihydroxyl groups attached to the surface of the $Fe_3O_4$-NPs are then undergo oxidation to form quinones, facilitated by an oxidative process causing hydrogen losses. Eventually, the $Fe_3O_4$-NPs become stabilized through the concurrent formation of quinones by the end of the reaction.

## 3.6 | Catalytic degradation of MO measurements

Moreover, UV-vis spectroscopy was employed to examine the degradation of MO both with and without the presence of the catalyst, *H. sabdariffa*/$Fe_3O_4$-NPs (Figure 7). Figure 7a shows the % degradation of MO dye with the presence of *H. sabdariffa*/$Fe_3O_4$-NPs (77.82%) is higher than without the presence of catalyst which revealed a significant reduction in MO concentration upon exposure to the *H. sabdariffa*/$Fe_3O_4$-NPs. The plot of the natural logarithm of the ratio of initial concentration to the concentration at the time $t$ ($[A_o/A_t]$) against time provides crucial information about the degradation kinetics and the reaction order. The plot of $\ln([A_o])/([A_t])$ versus time gives a straight line (Figure 7b), indicating that the concentration of MO gradually decreases and that this reaction follows pseudo-first-order kinetics with a rate constant of 0.0328 $s^{-1}$ ($R^2 = 0.9866$). The Langmuir

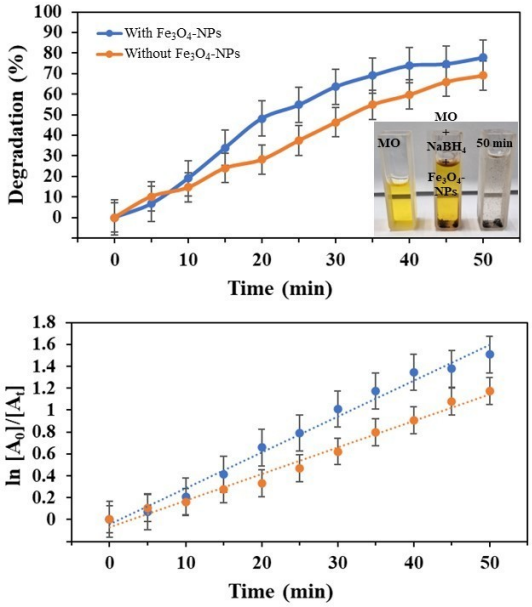


**FIGURE 7** (a) The plot of percent degradation versus time and (b) The plot of $\ln([A_0])/([A_t])$ versus time for degradation of MO.

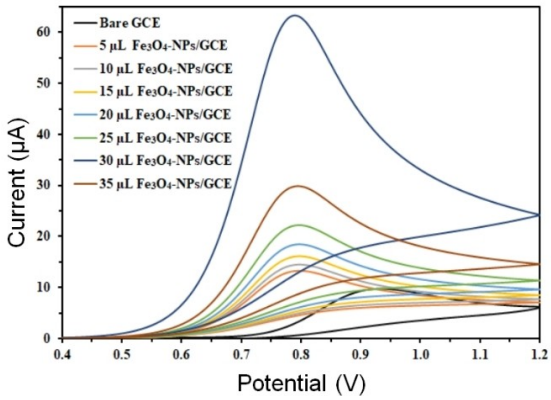


**FIGURE 8** CVs of bare GCE (black curve) and prepared $Fe_3O_4$-NPs/GCE for different volume drop cast (5 to 35 µL) in the presence of 1 mM $NO_2^-$ and 0.1 M KCl solution.

isotherm model accurately described the equilibrium behaviour of adsorption, showing that the pseudo-first-order model was the best fit for the adsorption kinetics compared to other models [49]. The observed narrow distribution and average particle size of $5 \pm 2$ nm for the *H. sabdariffa*/$Fe_3O_4$-NPs, as revealed by FESEM and TEM imaging, likely contribute to their enhanced catalytic activity. The structural characteristics of these nanoparticles play a pivotal role in facilitating efficient dye degradation, validating their potential for environmental remediation applications.

The catalytic efficiency of *H. sabdariffa*/$Fe_3O_4$-NPs was compared to previously reported catalyst in MO reduction (Table 1). The comparison revealed that *H. sabdariffa*/$Fe_3O_4$-NPs exhibit almost equivalent catalytic efficiency in terms of reaction time compared to previously documented catalyst. Additionally, when assessed against other nano-catalysts documented in the literature, the magnetic properties of the *H. sabdariffa*/$Fe_3O_4$-NPs allow for effortless separation from the reaction mixture without the need for filtration. Moreover, the synthesized nano-catalyst displayed stability, recyclability, and exceptional catalytic performance.

## 3.7 | Electrochemical sensing of $NO_2^-$

### 3.7.1 | Electrocatalytic studies

The electrocatalytic behaviour of *H. sabdariffa*/$Fe_3O_4$-NPs in $N_2$ saturated 0.1 M KCl solution in the presence of 1 mM $NO_2^-$ at a scan rate 50 $mVs^{-1}$ is shown in Figure 8. The CVs were scanned at the potential range of 0.4–1.2 V, which corresponds to the $NO_2^-$ oxidation peak potential. Based on Figure 8, the bare GCE response toward the oxidation of $NO_2^-$ was weak and broad at an irreversible oxidation peak around 0.9 V. This is due to the slow electron transfer kinetics of the $NO_2^-$ oxidation process [53]. On the other hand, the oxidation current peak of $Fe_3O_4$-NPs/GCE is higher than the bare GCE. This indicates that $NO_2^-$ can be oxidized over the $Fe_3O_4$-NPs. Besides, it can be seen from Figure 8 that the oxidation peak potential shifts towards a lower potential when *H. sabdariffa*/$Fe_3O_4$-NPs/GCE are used, compared with

**TABLE 1** Comparison of various catalyst used for degradation of MO.

| Adsorbent | Size (nm) | Time (min) | % Degradation | Ref. |
|---|---|---|---|---|
| H. sabdariffa/$Fe_3O_4$-NPs | ~5 | 50 | 77.82 | This work |
| α-$Fe_2O_3$ synthesized using glucose | 27.25 | 100 | 82.17 | [17] |
| α-$Fe_2O_3$ synthesized using sucrose | 6.13 | | 95.31 | |
| PS-$Fe_3O_4$ MNPs | 20–30 | 60 | 96 | [50] |
| $Fe_3O_4$/$Ti_2O$ | ~30 | 60 | 90.3 | [51] |
| $MoS_2$/MMT | 26300 | 120 | 98.6 | [52] |

bare GCE, indicating the significant impact of these NPs on electrocatalytic behaviour. $Fe_3O_4$-NPs can introduce several advantages characteristics such as enhanced conductivity, increased surface area, and tailored catalytic properties [1], all of which contribute to altering the electrode potential. Seven volumes of $Fe_3O_4$-NPs were investigated to determine the best drop cast volume. According to Figure 8, the best volume of NPs to detect $NO_2^-$ is 30 μL.

The $NO_2^-$are oxidised to the nitrate ions ($NO_3^-$) during the electrooxidation process, as proposed by Etesami and Mohamed in 2016 [54]. The anodic oxidation of $NO_2^-$ which is likely to involve the formation of nitrogen dioxide ($NO_2$) as a first step, then followed by the disproportionation reaction of $NO_2$:

$$2NO_2^- \rightleftharpoons 2NO_2 + 2e^-$$

$$2NO_2 + H_2O \rightarrow NO_2^- + NO_3^- + 2H^+$$

$$NO_2^- + H_2O \rightarrow NO_3^- + 2H^+ + 2e^-$$

During the electrooxidation process, $Fe_3O_4$-NPs can interact with $NO_2^-$ to form the complex of $Fe_3O_4$–$NO_2^-$. This complex electrochemically oxidized to form $Fe_3O_4^+$ and $NO_2$ before being converted to $Fe_3O_4$ and $NO_3^-$as follows:

$$Fe_3O_4 + NO_2^- \rightarrow Fe_3O_4 - NO_2^-$$

$$Fe_3O_4 - NO_2^- \rightarrow Fe_3O_4^+ - NO_2 + 2e^-$$

$$Fe_3O_4^+ - NO_2 + H_2O \rightarrow Fe_3O_4 + NO_3^- + 2H^+$$

### 3.7.2 | Amperometry detection of $NO_2^-$

The response of the $NO_2^-$ on the modified electrode were determined using the amperometry $i-t$ technique. Figure 9a depicts the typical current and time characteristics of $Fe_3O_4$-NPs/GCE for the addition of various concentrations of $NO_2^-$ with a working potential of 0.8 V. The sensors reach 90% of the steady-state current in 3 seconds, indicating that $NO_2^-$ diffuses quickly on the electrode surface. The limit of quantification (LOQ) and limit of detection (LOD) of the modified electrode were calculated. The calibration curve in Figure 9b shows a linear section of 0.5–7.5 mM for the response to $NO_2^-$ with the linear regression equation; $I = 349.24$ ($\mu A.mM^{-1}.cm^{-2}$) $+149.09$ with $R^2$ value of 0.9962, LOD value of 0.29 μM, and LOQ value of 0.98 μM. Table 2 summarizes the performance of various modified

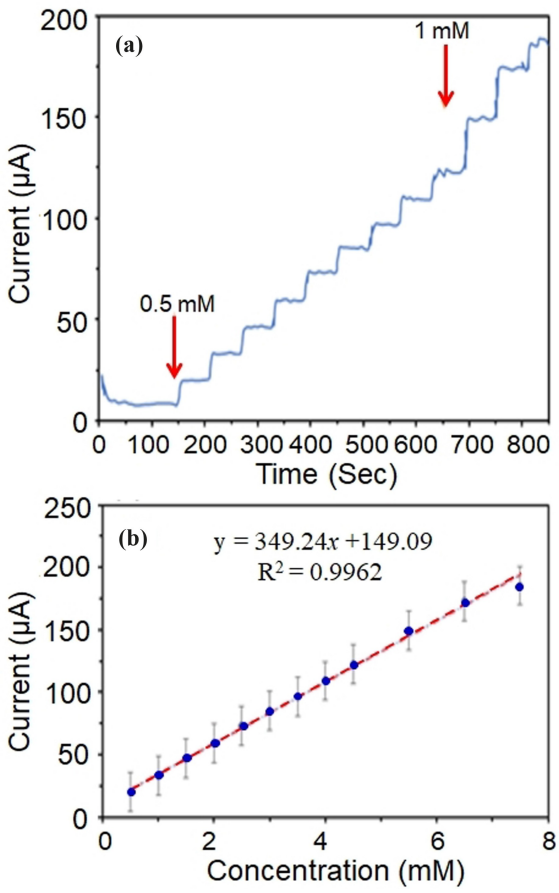


**FIGURE 9** Amperometric responses of the $Fe_3O_4$-NPs/GCE at an applied potential 0.8 V to various concentration of $NO_2^-$ from 0.5–1 mM. (b) The corresponding calibration plot for the $Fe_3O_4$-NPs/GCE.

electrodes based on $Fe_3O_4$. The results showed that the LOD, linear range and sensitivity of $Fe_3O_4$/GCE are comparable to or surpass those of other modified electrodes for $NO_2^-$ determination. The use of *H. sabdariffa*/$Fe_3O_4$-NPs in our $NO_2^-$ sensor represents a novel approach due to their unique electrochemical properties, including high surface area (due to the small size of the NPs) and superior stability. This innovation provides a cost-effective and environmentally friendly alternative to traditional materials used in electrochemical sensors. Hence, future work will focus on testing the sensor in medical, food, and environmental samples to establish its practical utility.

### 3.7.3 | Repeatability, reproducibility, and stability

Repeatability, reproducibility, and stability of the modified electrodes were investigated by voltammetry measurement and reported in terms of relative standard

**TABLE 2** Comparison of the fabricated Fe3O4-NPs/GCE with previously $NO_2^-$ sensors.

| Electrode | Size of NPs (nm) | Sensitivity | Linear range (μM) | LOD (μM) | Ref. |
|---|---|---|---|---|---|
| $Fe_3O_4$-NPs/GCE | 5 | 349.24 μA.mM$^{-1}$cm$^{-2}$ | 500–7500 | 290 | This work |
| PDDA-$Fe_3O_4$/Cys/MWCNTs/GC | 20–25 | – | 7.49–3330 | 0.846 | [33] |
| $Fe_3O_4$NPs/CILE | 10 | 0.0402 μA.μM$^{-1}$ | 10–900 | 0.7 | [53] |
| PEDOT/$Fe_3O_4$-CNCC/GCE | 10 | – | 0.0005–2.5 | 0.10 | [55] |
| Au@$Fe_3O_4$/Cys/GCE | 40–80 | – | 0.0036–10 | 0.82 | [56] |
| Pd/$Fe_3O_4$/polyDOPA/RGO/GCE | 8 | – | 2.5–6470 | 0.5 | [57] |
| $Fe_3O_4$/r-GO/GC | ~20 | 0.226 A.M$^{-1}$cm$^{-2}$ | 6–92 | 0.3 | [58] |
| Ag–$Fe_3O_4$–GO/GCE | 100 | 426 μA.mM$^-$ cm$^{-2}$ | 720–8150 | 0.17 | [59] |

deviation (RSD). The repeatability analysis was performed by using 10 sequentially prepared electrodes for 1.0 mM $NO_2^-$ in 0.1 M KCl solution. The resulting current values were obtained, and the RSD was found to be 4.50 %, indicating strong repeatability. The RSD value for the currents obtained from five identically modified electrodes was 3.81 %, indicating that the results could be reproducible. The stability of the modified electrode has also been examined for 21 days (Figure 10). After 3 weeks, the modified electrode retained about 65 % of its initial response, which can be attributed to good electrode stability ($I_0$ and $I_t$ was the response current in the first and subsequent days, respectively).

### 3.7.4 | Interference study

In some cases, interference with others unwanted elements can be fixed by determining the oxidation peak [53]. Possible interference for the detection of $NO_2^-$ at $Fe_3O_4$-NPs/GCE was investigated by addition of some common ions such as $SO_4^{2-}$, $NO_3^-$, and $Cl^-$ solution in the presence of 1.0 mM $NO_2^-$ (Figure 11). The results indicate that the mentioned ions did not show interference.

## 4 | CONCLUSION

In conclusion, the utilization of *H. sabdariffa* leaf extract as a green and sustainable means for the synthesis of $Fe_3O_4$-NPs has yielded promising outcomes. The characterized $Fe_3O_4$-NPs exhibited remarkable magnetic, structural, and morphological properties, validating their potential across multiple applications. The catalytic prowess of *H. sabdariffa*/$Fe_3O_4$-NPs in the degradation of MO dye showcased not only their catalytic efficiency but also their potential in environmental remediation. The $Fe_3O_4$-NPs generated displayed a narrow size distribution and an average particle dimension of 5 ± 2 nm, a pivotal element bolstering their catalytic effectiveness. factor contributing to their enhanced catalytic activity. Investigation unveiled that the breakdown of MO

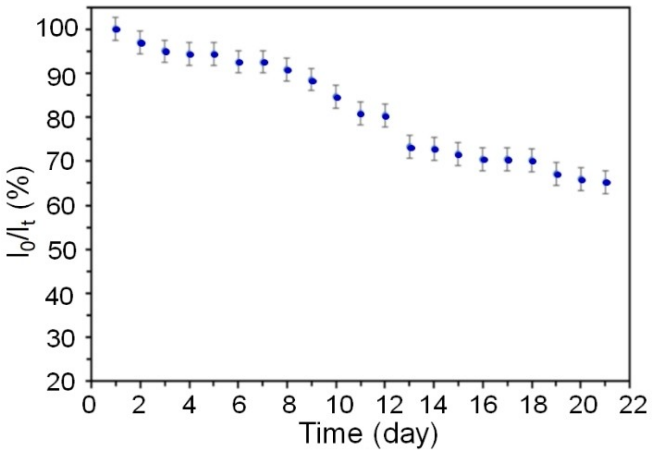


**FIGURE 10** The stability of $Fe_3O_4$-NPs/GCE over a three-week period in a 0.1 M KCl solution containing 1 mM $NO_2^-$, held at 0.8 V versus SCE.

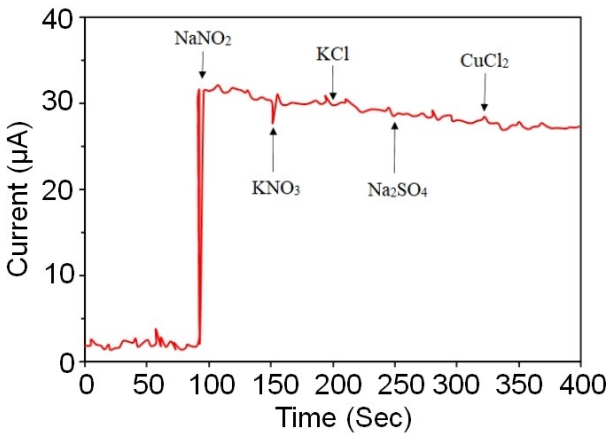


**FIGURE 11** $Fe_3O_4$-NPs/GCE interference test with 1 mM $NO_2^-$ in the presence of $KNO_3$, KCl, $Na_2SO_4$, $CuCl_2$.

adhered to pseudo-first-order kinetics, with a rate constant of 0.0328 $s^{-1}$, underscoring the notable catalytic efficacy of these NPs. Furthermore, the electrochemical sensing capability of the modified GCE with *H. sabdariffa*/$Fe_3O_4$-NPs demonstrated high sensitivity and reproducibility in detection of $NO_2^-$. The modified sensor exhibited a linear relationship between the anodic peak current of $NO_2^-$ within the range of 0.5–7.5 mM, achieving a commendable LOD of 0.29 μM, and a detection sensitivity of 349.24 $\mu A.mM^{-1}cm^{-2}$. This electrochemical sensing capability holds promise for applications in various fields, including medical diagnostics, food safety, and environmental monitoring. In essence, the findings presented in this study not only contribute to the expanding range of environmentally friendly nanoparticle synthesis but also highlight the versatile applications of these $Fe_3O_4$-NPs in catalytic degradation and electrochemical sensing, paving the way for sustainable and innovative solutions in diverse fields.

## AUTHOR CONTRIBUTIONS

The role of each author in the writing of this paper is listed in order. Conceptualization, S. H. M. Taib, P. M. Nia, R. R. Ali, Z. Izadiyan, Z. I. Tarmizi, and K. Shameli; methodology, S. H. M. Taib, P. M. Nia, and K. Shameli; project implementation, S. H. M. Taib, P. M. Nia, and K. Shameli; validation, S. H. M. Taib, P. M. Nia, and K. Shameli; formal analysis, S. H. M. Taib, P. M. Nia, and K. Shameli; investigation, P. M. Nia, R. R. Ali, Z. Izadiyan, Z. I. Tarmizi, and K. Shameli; resources, P. M. Nia, and K. Shameli; writing—original draft preparation, H. M. Taib, P. M. Nia, and K. Shameli; writing—review and editing, H. M. Taib, and K. Shameli; visualization, Z. Izadiyan, Z. I. Tarmizi, and K. Shameli; supervision, K. Shameli; project administration, K. Shameli.; funding acquisition, R. R. Ali, P. M. Nia, and K. Shameli. All authors have read and agreed to the published version of the manuscript.

## ACKNOWLEDGMENTS

The authors would like to thank the Technical University of Munich for facilitating this publication. The authors would like to gratefully acknowledge Siti Husnaa Mohd Taib which is a Researcher under the postdoctoral fellowship scheme for this project with the title: “Electrochemical detection of Covid-19 by Graphene Decorated with Gold Nanoparticle Modified Electrode”. The authors express their gratitude to the ChECA i-Kohza laboratory at the MJIIT and the CHE for granting access to their laboratory facilities.

## CONFLICT OF INTEREST STATEMENT

Authors declare that all data can be shared and accessed by the permission of the journal publication rules.

## DATA AVAILABILITY STATEMENT

Data sharing is not applicable to this article as no new data were created or analysed in this study.

## ORCID

*Kamyar Shameli* http://orcid.org/0000-0002-3955-4604

## REFERENCES

1. M. D. Nguyen, H. V. Tran, S. Xu, T. R. Lee, *Appl. Sci.* **2021**, *11*(*23*), 11301, 1–34.
2. A. D. Olaitan, S. Ward, L. F. Barnes, J. R. Yount, B. A. Zanca, J. I. Schwieg, A. L. McCoy, K. S. Molek, *Rapid Commun. Mass Spectrom* **2018**, *32*, 1887–1896.
3. M. Imran Din, A. Rani, *Int. J. Anal. Chem.* **2016**, *2016*, 1–14.
4. D. Maity, P. Chandrasekharan, C.-T. Yang, K.-H. Chuang, B. Shuter, J.-M. Xue, J. Ding, S.-S. Feng, *Nanomedicine* **2010**, *5* (2010) 1571–1584.
5. H. El Ghandoor, H. M. Zidan, M. M. H. Khalil, M. I. M. Ismail, *Int. J. Electrochem. Sci.* **2012**, *7* (2012) 5734–5745.
6. R. Vijayakumar, Yu. Koltypin, I. Felner, A. Gedanken, *Mater. Sci. Eng. A* **2000**, *286*, 101–105.
7. J. Xu, H. Yang, W. Fu, K. Du, Y. Sui, J. Chen, Y. Zeng, M. Li, G. Zou, *J. Magn. Magn. Mater.* **2007**, *309*, 307–311.
8. W. Zhang, F. Shen, R. Hong, *Particuology* **2011**, *9* (2), 179–186.
9. C. Han, W. Cai, W. Tang, G. Wang, C. Liang, *J. Mater. Chem.* **2011**, *21* (30), 11188–11196.
10. F. Moradnia, S. T. Fardood, A. Zarei, S. Heidarzadeh, A. Ramazani, M. Sillanpää, *Iran. J. Catal.* **2024**, *14* (*1*), 142401, 1–24
11. S. Taghavi Fardood, F. Moradnia, F. Yekke Zare, S. Heidarzadeh, M. Azad Majedi, A. Ramazani, M. Sillanpää, K. Nguyen, *Sci. Rep.* **2024**, *14*, 6755.
12. E. J. Al-Kalifawi, *J. Nat. Sci.* **2015**, *5* (20), 125–135.
13. S. Venkateswarlu, Y. S. Rao, T. Balaji, B. Prathima, N. V. V. Jyothi, *Mater Lett.* **2013**, *100*, 241–244.
14. I. Da-Costa-Rocha, B. Bonnlaender, H. Sievers, I. Pischel, M. Heinrich, *Food Chem.* **2014**, *165*, 424–443.
15. N. H. Abd Karim, M. Ahmad, M. Osman, Herman, A. M. Mokhtar, *Sains Malays.* **2008**, *37* (1), 59–63.
16. C. Umamaheswari, A. Lakshmanan, N. S. Nagarajan, *J. Photochem. Photobiol. B.* **2018**, *178*, 33–39.
17. R. K. Shah, *Arab. J. Chem.* **2023**, *16* (*2*), 104444, 1–10.
18. H. Kumari, S. Suman, R. Ranga, S. Chahal, S. Devi, S. Sharma, S. Kumar, P. Kumar, S. Kumar, A. Kumar, R. Parmar, *Water Air Soil Pollut.* **2024**, *234* (349), 1–46.
19. P. Poormoghadam, A. Larki, S. Rastegarzadeh, *Anal. Methods.* **2015**, *7*, 8655–8662.
20. R. Roila, R. Branciari, B. Staccini, D. Ranucci, D. Miraglia, M. S. Altissimi, M. L. Mercuri, N. M. Haouet, *Ital. J. Food Saf.* **2018**, *7*(3), 7692.
21. H. Z. Mousavi, H. Shirkhanloo, *J. Serb. Chem. Soc.* **2009**, *74*, 985–992.
22. L. Wu, Z.-M. Song, Y. Chen, H. Zhu, Z. Li, Y. Gao, J. Yang, Y. Hung, *Asian J. Chem.* **2013**, *25* (17), 9520–9522.

23. Z. Lin, X. Dou, H. Li, Y. Ma, J. M. Lin, *Talanta* **2015**, *132*, 457–462.
24. X. Wang, E. Adams, A. Van Schepdael, *Talanta* **2012**, *97*, 142–144.
25. R. Mo, X. Wang, Q. Yuan, X. Yan, T. Su, Y. Feng, L. Lv, C. Zhou, P. Hong, S. Sun, Z. Wang, C. Li, *Sensors* **2018**, *18* (*7*), 1986, 1–12.
26. C. Zou, B. Yang, D. Bin, J. Wang, S. Li, P. Yang, C. Wang, Y. Shiraishi, Y. Du, *J. Colloid Interface Sci.* **2017**, *488*, 135–141.
27. D. K. Yadav, V. Ganesan, P. K. Sonkar, R. Gupta, P. K. Rastogi, *Electrochim. Acta* **2016**, *200*, 276–282.
28. B. O. Agboola, K. I. Ozoemena, T. Nyokong, *Electrochim. Acta* **2006**, *51*, 6470–6478.
29. C. A. Caro, F. Bedioui, J. H. Zagal, *Electrochim Acta* **2002**, *47*, 1489–1494.
30. X. Song, L. Gao, Y. Li, L. Mao, J. H. Yang, *Anal. Methods* **2017**, *9*(21), 3166–3171.
31. J. Jiang, W. Fan, X. Du, *Biosens. Bioelectron.* **2014**, *51*, 343–348.
32. X. Wang, H. Li, M. Wu, S. L. Ge, Y. Zhu, Q. J. Wang, P. G. He, Y. Z. Fang, *Chinese J. Anal. Chem.* **2013**, *41* (8), 1232–1237.
33. J. Qu, Y. Dong, Y. Wang, H. Xing, *Sens. Biosensing Res.* **2015**, *3*, 74–78.
34. V. Urbanova, M. Magro, A. Gedanken, D. Baratella, F. Vianello, R. Zboril, *Chem. Mater.* **2014**, *26*, 6653–6673.
35. S. Xuan, Y. X. J. Wang, J. C. Yu, K. C. F. Leung, *Chem. Mater.* **2009**, *21*, 5079–5087.
36. M. Mahdavi, M. Ahmad, M. J. Haron, F. Namvar, B. Nadi, M. Z. Ab Rahman, J. Amin, *Molecules* **2013**, *18*, 7533–7548.
37. V. Patsula, D. Horák, J. Kučka, H. Macková, V. Lobaz, P. Francová, V. Herynek, T. Heizer, P. Páral, L. Šefc, *Sci. Rep.* **2019**, *9*, 1–12.
38. N. Bala, S. Saha, M. Chakraborty, M. Maiti, S. Das, R. Basu, P. Nandy, *RSC Adv.* **2015**, *5*, 4993–5003.
39. F. Moradnia, S. Taghavi Fardood, A. Ramazani, *Appl. Organomet. Chem.* **2024**, *38* (3), e7315.
40. M. T. Kiani, A. Ramazani, S. Taghavi Fardood, *Appl. Organomet. Chem.* **2023**,*37* (4), e7053.
41. M. Mahdavi, F. Namvar, M. Ahmad, R. Mohamad, *Molecules* **2013**, *18*, 5954–5964.
42. H. A. Eivari, A. Rahdar, H. Arabi, *Int. J. Sci. Eng. Investig.* **2012**, *1* (3), 70–72.
43. E. H. Ismail, M. M. H. Khalil, F. A. Al Seif, F. El-Maghdoub, *Progress in Nanotechnology and Nanomaterials (PNN)* **2014**, *3*, 1–12.
44. S. Sharaf, A. Higazy, A. Hebeish, *Int. J. Biol. Macromol.* **2013**, *59*, 408–416.
45. R. Świsłocka, *Spectrochim. Acta A Mol. Biomol. Spectrosc.* **2013**, *100*, 21–30.
46. A. M. Awwad, N. M. Salem, *J. Nanosci. Nanotechnol.* **2012**, *2* (6), 208–213.
47. Y. P. Yew, K. Shameli, M. Miyake, N. B. A. Khairudin, S. E. Mohamad, H. Hara, M. F. Mad Nordin, K. X. Lee, *IEEE Trans. Nanotechnol.* **2018**, *16* (6), 1047–1052.
48. S. H. Mohd Taib, K. Shameli, P. Moozarm Nia, M. Etesami, M. Miyake, R. Rasit Ali, E. Abouzari-Lotf, Z. Izadiyan, *J. Taiwan Inst. Chem. Eng.* **2019**, *95*, 616–626.
49. B. Farasati Far, M. R. Naimi-Jamal, M. Jahanbakhshi, S. A. Khalafvandi, M. Alian, D. Razeghi Jahromi, *J. Mol. Liq.* **2024**, *395*, 123839.
50. C. Prasad, G. Yuvaraja, P. Venkateswarlu, *J. Magn. Magn. Mater.* **2017**, *424*, 376–381.
51. N. I. Mohd Razip, K. M. Lee, C. W. Lai, B. H. Ong, *Mater. Res. Express* **2019**, *6*, 075517.
52. L. Yang, Q. Wang, J. R. Rangel-Mendez, F. Jia, S. Song, B. Yang, *Mater. Chem. Phys.* **2020**, *246*, 122829.
53. G. Absalan, M. Akhond, A. Bananejad, H. Ershadifar, *J. Iran. Chem. Soc.* **2015**, *12*, 1293–1301.
54. M. Etesami, N. Mohamed, *J. Anal. Chem.* **2016**, *71* (2), 185–194.
55. G. Xu, M. Zhang, X. Yu, *Acta Chim. Slov.* **2018**, *65*, 502–511.
56. C. Yu, J. Guo, H. Gu, *Electroanalysis* **2010**, *22*, 1005–1011.
57. Z. Zhao, Z. Xia, C. Liu, H. Huang, W. Ye, *Electrochim. Acta* **2017**, *256*, 146–154.
58. H. Teymourian, A. Salimi, S. Khezrian, *Biosens. Bioelectron.* **2013**, *49*, 1–8.
59. B. Q. Li, F. Nie, Q. L. Sheng, J. Zheng, *Chem. Pap.* **2015**, *69*, 911–920.


**How to cite this article:** S. Husnaa Mohd Taib, P. Moozarm Nia, R. Rasit Ali, Z. Izadiyan, Z. Izzah Tarmizi, K. Shameli, *Electroanalysis* **2024**, *36*, e202300422. https://doi.org/10.1002/elan.202300422